

A Supernova Remnant Counterpart for HESS J1832-085

NIGEL I. MAXTED,¹ M. D. FILIPOVIĆ,² N. HURLEY-WALKER,³ I. BOJČIĆ,² G. P. ROWELL,⁴ F. HABERL,⁵ A. J. RUITER,¹
I. R. SEITENZAHL,¹ F. PANTHER,¹ G. F. WONG,^{2,6} C. BRAIDING,⁶ M. BURTON,⁷ G. PÜHLHOFER,⁸ H. SANO,⁹ Y. FUKUI,⁹
M. SASAKI,¹⁰ W. TIAN,^{11,12} H. SU,¹¹ X. CUI,¹¹ D. LEAHY,¹³ AND P. J. HANCOCK^{3,14}

¹*School of Science, The University of New South Wales, Australian Defence Force Academy, Canberra 2610, Australia*

²*Western Sydney University, Locked Bag 1797, Penrith, NSW 2751, Australia*

³*International Centre for Radio Astronomy Research, Curtin University, Bentley, WA 6102, Australia*

⁴*School of Physical Sciences, The University of Adelaide, Adelaide 5005, Australia*

⁵*Max-Planck-Institut für extraterrestrische Physik, Giessenbachstraße, 85748 Garching, Germany*

⁶*School of Physics, The University of New South Wales, Sydney 2052, Australia*

⁷*Armagh Observatory and Planetarium, College Hill, Armagh BT61 9DG, UK*

⁸*Institut für Astronomie und Astrophysik, Universität Tübingen, 72076 Tübingen, Germany*

⁹*Department of Physics, Nagoya University, Furo-cho, Chikusa-ku, Nagoya 464-8601, Japan*

¹⁰*Dr. Karl Remeis Observatory and ECAP, Universität Erlangen-Nürnberg, Sternwartstr. 7, 96049 Bamberg, Germany*

¹¹*National Astronomical Observatories, CAS, Beijing 100012, China*

¹²*University of Chinese Academy of Sciences, Beijing 100049, China*

¹³*Department of Physics & Astronomy, University of Calgary, Calgary, Alberta T2N 1N4, Canada*

¹⁴*ARC Centre of Excellence for All-sky Astrophysics (CAASTRO)*

(Received July 3, 2019; Revised August 18, 2019; Accepted August 23, 2019)

Submitted to ApJ

ABSTRACT

We examine the new Galactic supernova remnant (SNR) candidate, G23.11+0.18, as seen by the Murchison Widefield Array (MWA) radio telescope. We describe the morphology of the candidate and find a spectral index of -0.63 ± 0.05 in the 70-170 MHz domain. A coincident TeV gamma-ray detection in High-Energy Stereoscopic System (HESS) data supports the SNR nature of G23.11+0.18 and suggests that G23.11+0.18 is accelerating particles beyond TeV energies, thus making this object a promising new cosmic ray hadron source candidate. The remnant cannot be seen in current optical, infrared and X-ray data-sets. We do find, however, a dip in CO-traced molecular gas at a line-of-sight velocity of $\sim 85 \text{ km s}^{-1}$, suggesting the existence of a G23.11+0.18 progenitor wind-blown bubble. Furthermore, the discovery of molecular gas clumps at a neighbouring velocity towards HESS J1832-085 adheres to the notion that a hadronic gamma-ray production mechanism is plausible towards the north of the remnant. Based on these morphological arguments, we propose an interstellar medium association for G23.11+0.18 at a kinematic distance of $4.6 \pm 0.8 \text{ kpc}$.

Keywords: ISM: individual objects: G23.11+0.18 – HESS J1832-085 – ISM: supernova remnants – Radio continuum: – ISM: supernova remnants – gamma-rays: – ISM: cosmic rays – ISM: molecules

1. INTRODUCTION

Supernova remnants (SNRs) are key candidates in the search for the Galaxy's sources of cosmic ray hadrons up to energies of several PeV. Investigations of cosmic-ray (CR) origin are partly enabled by gamma-ray instruments, which can trace distant populations of high-energy particles through interaction byproducts. Similarly, non-thermal radio

continuum emission traces populations of high energy electrons as they gain and then lose energy in the shells of SNRs. It follows that an inherent connection between radio emission and gamma-rays exists in the non-thermal spectra of SNRs, thus together, these two energy-windows can deliver constraints on particle acceleration and are complimentary in identifying SNRs (e.g. [H.E.S.S. Collaboration et al. 2018a](#)). We place the new supernova remnant G23.11+0.18 (the topic of this paper) and coincident TeV gamma-ray source, HESS J1832–085, in this category.

In several middle-aged ($\sim 10^4$ yr) SNRs, the Fermi gamma-ray space telescope successfully measured a distinctive high-energy spectral feature that is related to CR proton interactions with gas - the so-called ‘pion-bump’ ([Ackermann et al. 2013](#)) from proton-proton (p-p) interactions that create neutral pions, which subsequently decay into gamma-ray photons. The process naturally connects interstellar medium (ISM) gas and gamma-rays, and has allowed several other middle-aged SNRs to be identified as past CR accelerators through the observed overlap between TeV gamma-rays and molecular gas, which is impacted by high-energy protons diffusing away from their acceleration sites (e.g. [Aharonian et al. 2008](#); [Albert et al. 2007](#)). P-p interactions of CR protons diffusing away from a local source has also been invoked to explain an excess of gamma-ray emission from the Galactic Centre, given an energy-dependent distribution measured by High-Energy Stereoscopic System (HESS) ([Abramowski et al. 2016](#)).

Gamma-ray emission can also be created via the inverse-Compton mechanism, whereby high-energy electrons up-scatter low-energy photons to gamma-ray energies. The gamma-ray mechanism of some young shell-type gamma-ray-bright SNRs is presently the subject of vigorous debate. Attempts to replicate global gamma-ray spectra may favour electrons as the primary dominant particle triggering gamma-ray emission – a so-called ‘leptonic’ model (e.g. see [Acero et al. 2015a](#)), while conversely, good correspondences between ISM gas density and gamma-ray flux is suggestive of CR proton interactions – a so-called ‘hadronic’ model in the very same young objects ([Fukui et al. 2012](#); [Fukuda et al. 2014](#); [Fukui et al. 2017](#), for RX J1713.7–3946, HESS J1731–347 and Vela Jr, respectively)¹. In many cases, the absence of direct shock tracers (such as SiO emission for example, [Nicholas et al. 2012](#)) means that proposed ISM associations primarily rely on matching high energy features to gas structure.

Extensive modeling has shown that a gamma-ray spectral shape similar to leptonic gamma-ray emission can plausibly be created by hadronic processes in the presence of an inhomogeneous and clumpy circumstellar medium (e.g. [Zirakashvili & Aharonian 2010](#); [Inoue et al. 2012](#); [Fukui et al. 2012](#); [Celli et al. 2018](#); [Inoue 2019](#)), hence resolving the two seemingly-conflicting lines of evidence. In contrast with the aforementioned escaping CR scenario, this would be hadronic gamma-ray emission from within the SNR shell boundary rather than outside the shell. Another way to resolve the leptonic high energy spectral shape of young shell-type gamma-ray SNRs with the observed gas/gamma-ray correlation characteristic of hadronic gamma-ray emission may be to model electron injection as a function of ISM density (e.g. as suggested in [Susch et al. 2018](#)). The nature of gamma-ray emission (lepton or hadron-dominated) from young SNRs is a matter of ongoing debate.

Regardless of the dominant gamma-ray emission mechanism, acceleration of electrons to TeV energies is occurring in young SNRs, as evidenced by synchrotron X-ray emission from young SNR shocks. The non-thermal spectrum largely follows the energy spectrum of the local electron population, often extending down to radio frequencies. In this way, the radio, X-ray and gamma-ray skies are inherently linked, and a characterisation of the radio spectrum can provide constraints on electron acceleration within SNRs. The processes of proton acceleration are expected to be quite similar, so such constraints are also very relevant to investigations of CR origin, and either adjacent or embedded gas can help us form an understanding of the nature of associated gamma-ray emission (as is the case for the aforementioned examples of W28 and RX J1713.7–3946, respectively).

Finally, we note that the discovery of new Galactic SNRs generally, by any means, helps minimise the discrepancy observed between star formation rates and the population of known SNRs (e.g. see [Brogan et al. 2006](#); [Stupar et al. 2007a,b](#); [Ergin et al. 2017](#)).

In this paper, we investigate the new SNR G23.11+0.18 in the context of the search for Galactic CR hadron sources that are not necessarily expected to have clear shock-interaction signatures in an inhomogeneous interstellar medium. In Section 1.1, we summarise the current knowledge of the G23.11+0.18 region. In Section 2, we outline the multi-wavelength (MWL) data analysed in this study, and in Section 3 we present new images and spectra of G23.11+0.18 before discussing our search for MWL counterparts. We conclude by proposing a connection between G23.11+0.18, HESS J1832–085 and the interstellar medium.

¹ However, evidence for a dominant hadronic component for HESS J1731–347 only exists for the 5.2-6 kpc distance solution, as opposed to the 3.2 kpc solution favoured by the [Cui et al. \(2016\)](#) model and explicitly derived in [Maxted et al. \(2018a\)](#)

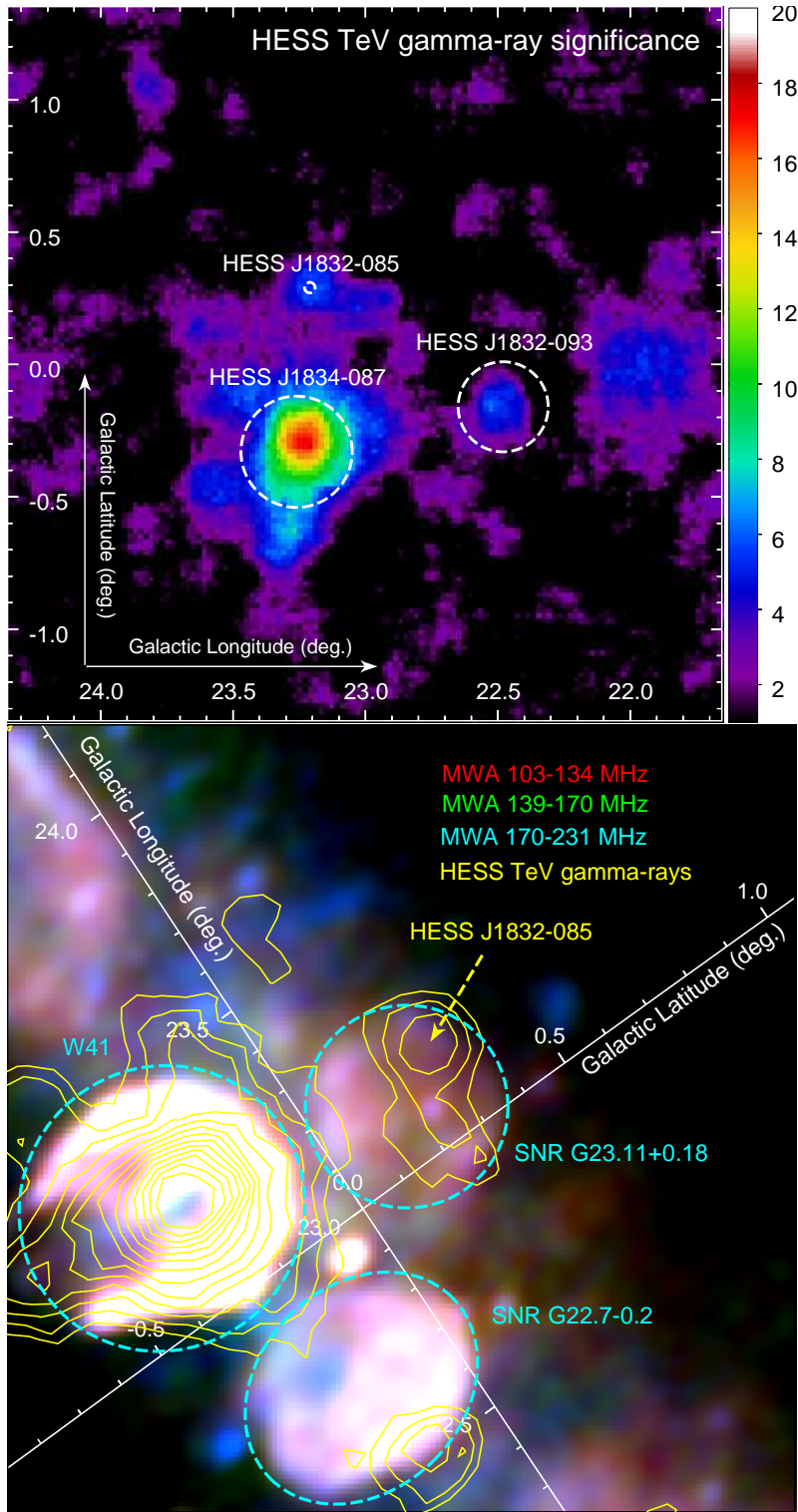


Figure 1. Top: HESS telescope Galactic Plane Survey image of TeV gamma-ray emission significance towards the HESS J1834–087 region (see Abdalla et al. 2018, for details). Previously established/known SNRs are marked with dashed circles. **Bottom:** 3-colour image of 3 sub-bands of Murchison Widefield Array radio continuum data (red:103-134 MHz, green:139-170 MHz, blue:170-231 MHz) towards the region containing the new SNR candidate G23.11+0.18. G23.11+0.18, composite PWN/SNR W41 and SNR G22.7-0.2 are indicated by dashed cyan ellipses. HESS TeV gamma-ray emission significance contours (Abdalla et al. 2018), starting at a 3σ level, are overlaid.

1.1. *The W41 region and HESS J1832–085*

Figure 1 is an image of gamma-ray emission towards HESS J1834–087 and the surrounding region (Abdalla et al. 2018). Bright gamma-ray emission from the composite SNR/pulsar-wind-nebula system, W41, is known as HESS J1834–087 and dominates the image. Several weaker gamma-ray sources exist nearby. To the centre-north is the unidentified ‘point-like’ gamma-ray source, HESS J1832–085. The HESS collaboration investigated a possible pulsar (PSR J1832–0836/MSP J1832–0836) origin for this source. Although the spin-down power is not considered sufficient to power such luminous gamma-ray emission, for millisecond pulsars that may have been ‘spun-up’ by accretion (e.g. Lee et al. 2018) the precise relationship between spin-down power and luminosity is unclear. We revisit this scenario in Section 3.5, after we examine HESS J1832–085 in light of a newly-discovered SNR (G23.11+0.18), as seen in Murchison Widefield Array (MWA) data in Section 3.1.

To the west of HESS J1834–087 is HESS J1832–093. Recent observations, strongly indicate a non-accreting binary origin for this gamma-ray emission (Eger et al. 2016; Mori et al. 2017). This is contrasted with initial investigations which suggested a possible association with the SNR G22.7–0.2 (HESS Collaboration et al. 2015). Su et al. (2014) previously identified a possible molecular cloud counterpart at 75–79 km s^{−1}, which was at the time suggested to be a target of CR hadrons accelerated in the shock of SNR G22.7–0.2. However, this SNR-cloud interaction origin for HESS J1834–087 is now disfavoured (HESS Collaboration et al. 2015). Su et al. (2014) also noted that the cloud² is a possible candidate for association with the W41 SNR and the H II region G022.760–0.485. Indeed, gas at this velocity is also considered in our examination of potential associations for the recently discovered SNR candidate G23.11+0.18 in Section 3.2.

2. OBSERVATIONS

In this paper we primarily utilise radio continuum data from the Murchison Widefield Array (MWA), TeV gamma-ray data from the High Energy Stereoscopic System (HESS) Galactic Plane Survey (Abdalla et al. 2018), molecular gas data from the FUGIN CO(1-0) survey (Umemoto et al. 2017) and X-ray data from the X-ray Multi-Mirror Mission (a.k.a *XMM-Newton*). Several instances of SNR candidate overlap with gamma-ray emission were present in a preliminary investigation carried out using MWA and HESS data. In this study we solely focus on one compelling source, the SNR candidate G23.11+0.18.

2.1. *MWA radio continuum*

The Murchison Widefield Array (MWA) is a collection of 2048 dual-polarisation dipole antennas situated in the Shire of Murchison in Western Australia, approximately 300 km from the small coastal town of Geraldton. The MWA is the low-frequency pre-cursor to the Square Kilometer Array (SKA) and is comprised of a central core of dipoles within a ~ 1.5 km region with extensions out to 3 km to cover longer baselines. The MWA has no moving parts such that the array is ‘steered’ electronically within 25° of sky (see Tingay et al. 2013, for details).

Data from the Galactic and Extragalactic All-sky Murchison Widefield Array (GLEAM) survey (Wayth et al. 2015) was processed to produce a data release covering covering $345^\circ < l < 60^\circ$, $180^\circ < l < 240^\circ$, $|b| \leq 10^\circ$ Hurley-Walker (2019a), which has an effective integration time of about 10 minutes per pixel. Hurley-Walker (2019b) examined this data for known Galactic SNR candidates, and Hurley-Walker (2019c) searched it for new SNRs, finding 26. The GLEAM data-set is sensitive to radio continuum emission at frequencies between 72 and 231 MHz and is made up of 20 bands with a channel bandwidth of 7.68 MHz. For faint objects, it is useful to combine the data into 4 bins: 72–103, 103–134, 139–170 and 170–231 MHz, with corresponding image Point Spread Functions (PSFs) of 5.2’, 3.9’, 2.9’ and 2.4’.

New GLEAM MWA data is complemented by archival data from the Bonn 11-cm (2.695 GHz) Survey with the Effelsberg Telescope (Reich et al. 1984). This is a single-dish survey covering $357.4 \leq l \leq 76^\circ$, $b \leq |1.5|$ with 4’3 resolution and 50 mK (20 mJy beam^{−1}) sensitivity³.

2.2. *HESS Gamma-rays*

The HESS telescope is a system of 5 ground-based Cherenkov light detectors operating in the Khomas Highland of Namibia at an altitude of 1800 m. The array consists of four 12 m diameter telescopes, operating from 2003, and

² The authors suggested a 4.4 ± 0.4 kpc distance and Scutum-Crux arm association for this cloud, but we suggest that a Norma-arm association beyond 70 km s^{−1} is more likely.

³ <http://www3.mpifr-bonn.mpg.de/survey.html>

one 28 m diameter telescope, operating since 2012. The five detectors observe Cherenkov light from showers of high energy particles produced by ~ 0.1 -100 TeV-energy gamma-ray photons interacting in the air above the dark Khomas Highland site.

The HESS Galactic Plane Survey utilised in this work is a compilation of 14 years of observations with the four 12 m-diameter telescopes. It has varying energy threshold and spatial resolution across the Milky Way, while the telescope is generally sensitive to photon energies larger than >200 GeV with a photon energy-reconstruction accuracy of $\sim 15\%$. The photon arrival direction reconstruction is accurate to within $\sim 0.08^\circ$ (Abdalla et al. 2018), which is the approximate angular resolution of resultant maps.

2.3. FUGIN CO(1-0)

FUGIN is an acronym for the FOREST Unbiased Galactic plane Imaging survey with the Nobeyama 45 m telescope, where FOREST is itself an acronym for the FOur-beam REceiver System on the 45-m Telescope (Minamidani et al. 2016). The Nobeyama telescope is located at an elevation of 1350 m in Minamimaki, near Nagano, Japan.

The Nobeyama telescope has a beam full-width half-maximum of $14''$ at 115 GHz, which results in a post-reduction CO(1-0) angular resolution of $20''$ and a $^{13}\text{CO}/\text{C}^{18}\text{O}(1-0)$ angular resolution of $21''$ for FUGIN survey data (Umemoto et al. 2017). The FUGIN CO(1-0) velocity resolution and beam efficiency are 1.3 km s^{-1} and 0.43 ± 0.02 , respectively.

As part of this investigation, FUGIN CO data is processed using Miriad software (Sault et al. 1995).

We note that a search for gas counterparts for Galactic SNRs detected in the GLEAM survey will be viable using the southern hemisphere Mopra Galactic Plane CO survey (Burton et al. 2013; Braiding et al. 2015, 2018) between longitudes of -110° and 11° . In the particular case of G23.11+0.18, the candidate falls outside of the Mopra survey coverage. Generally, we anticipate the Mopra and FUGIN surveys, in the southern and northern hemispheres, respectively, to be complementary in future studies of SNRs in the Galactic Plane.

2.4. XMM-Newton X-rays

We also examined XMM-Newton 0.2-4.5 keV X-ray emission data for signatures of the proposed SNR candidate. Approximately 30 ksec of XMM-Newton exposure were obtained in October 2007 towards the bright source AX J1832.3-0840. The three European Photon Imaging Camera (EPIC) instruments (Turner et al. 2001; Strüder et al. 2001) are operated simultaneously and cover a field of view of about $30'$ in diameter, encompassing a large fraction of G23.11+0.18.

AX J1832.3-0840 is most likely a magnetic cataclysmic variable (intermediate polar) or a high-mass X-ray binary. It shows X-ray pulsations with a period of ~ 1550 s discovered in the Advanced Satellite for Cosmology and Astrophysics (ASCA) data (Kaur et al. 2010, also see Gaia Collaboration et al. 2018).

We created XMM-Newton images following Sturm et al. (2013). After removal of two short background flares, the net exposure times for the three EPIC instruments⁴ were 26.0 ks, 28.6 ks and 28.8 ks for pn, MOS1 and MOS2, respectively.

The detection of a potential diffuse X-ray emission signal from SNR candidate G23.11+0.18 is hampered by high foreground absorption, which attenuates soft X-rays, and dust scattering halos around bright sources, particularly towards this dense and active part of the Galactic Plane. Assuming a visual extinction to reddening ratio of 3.1 (Schlafly & Finkbeiner 2011) and ~ 2.1 - $2.2 \times 10^{21} \text{ cm}^{-2}$ of foreground H column density per magnitude of visual extinction (Güver & Özel 2009; Zhu et al. 2017), the measured optical extinction⁵ of 35-40 A_V towards HESS J1832-085 implies a possible foreground absorption column density of up to 7 - $9 \times 10^{22} \text{ cm}^{-2}$. For such a column density, a typical SNR with thermal temperatures of 0.25-0.6 keV would have $>99\%$ of $\lesssim 5$ keV X-ray emission absorbed by photoelectric absorption, assuming solar elemental abundances in foreground gas. We note that some proportion of visual extinction may be attributable to gas associated with G23.11+0.18, as discussed in Section 3.3. The results of our X-ray investigation are discussed in Section 3.4.

3. RESULTS AND DISCUSSION

The SNR candidate, G23.11+0.18, is indicated in Figure 1, which shows three frequency bands of MWA data towards the Galactic plane centred on the SNR. In the following subsection, we summarise the radio continuum characteristics of G23.11+0.18, before a multi-wavelength investigation is outlined in subsequent subsections. We particularly focus

⁴ Two Metal-Oxide-Silicon detectors and a fully depleted PN CCD

⁵ <http://irsa.ipac.caltech.edu/applications/DUST/>

on the origin of the gamma-ray source HESS J1832–085, in the light of the discovery of G23.11+0.18. Finally, we propose and discuss the nature and distance of the new SNR candidate.

3.1. The G23.11+0.18 Radio Continuum

Images of four frequency bands of MWA radio continuum data are displayed in Figure 2. The proposed extent of non-thermal emission from the shell of the new SNR candidate, previously designated SNR G23.11+0.18 in Anderson et al. (2017) and independently discovered in our study, is indicated by a circle at centroid (l, b) of ($23.12^\circ, 0.19^\circ$ (RA (J2000), Dec (J2000): $\sim 18^h 32^m 29.7^s, -8^\circ 39' 12.9''$) and radius of $750''$ in Figure 1 and 2. We estimate the SNR radius (with conservative uncertainty) to be $700 \pm 50''$.

The apparent SNR shell is comprised of three broken segments in the highest frequency band (170–231 MHz). The largest segment spans a circular angle of approximately 90° in the south-east, and smaller arcs ($\sim 45^\circ$) of emission are present in the north-east and north-west (see Figure 2).

We noted the presence of a point source within the shell of G23.11+0.18, and searched for information on this source in other surveys. The 1st Alternative Data Release of the Tata Institute for Fundamental Research Giant Metrewave Radio Telescope Sky Survey (TGSS-ADR1; Intema et al. 2017) shows an unresolved source with total flux density $S = 805 \pm 80$ mJy at 150 MHz, while the National Radio Astronomy Observatory Very Large Array Sky Survey (NVSS; Condon et al. 1998) measures the same source with $S = 85.4 \pm 3.1$ mJy at 1400 MHz. NVSS has the best astrometry of these surveys and gives a position of RA = $18^h 32^m 32.25^s$, dec = $-08^d 38^m 54.5^s$ for the source. Combining the two flux density measurements yields a source with spectral index $\alpha = -1.00 \pm 0.05$. As the source is unresolved and has a steep spectral index, we do not believe it to be part of the shell itself. It is $3'$ from the centroid of G23.11+0.18, and could potentially be a radio-bright pulsar, potentially mis-aligned and thus not appearing in existing pulsar surveys of the region.

Alternatively, the source could be a radio galaxy with chance coincidence along the line-of-sight. Hurley-Walker et al. (2017) surveyed 24,402 square degrees of the sky over 72–231 MHz and created a catalogue of 307,456 radio sources at 200 MHz, with an estimated completeness of 98 % at 600 mJy, the flux density of the point source at this frequency. There are 27,628 sources with $S_{200\text{MHz}} > 0.6$ Jy, reducing to 1,163 for sources where α is also less than -1.1 . Therefore, the chance coincidence of any random radio galaxy lying anywhere within the shell is 13 %. This reduces to ≈ 0.6 % for any source lying within a radius of $3'$ from the shell centroid, or a steep-spectrum source lying anywhere within the shell. The chance of a steep-spectrum radio galaxy of the required flux density lying within $3'$ of the centroid is just 0.03 %.

The *Wide-field Infrared Survey Explorer* (WISE; Wright et al. 2010) surveyed the sky at 3.4, 4.6, 12, and $22 \mu\text{m}$, producing relatively high-resolution and high-sensitivity IR images of the entire sky. Radio galaxies selected at low frequencies and high flux densities ($S_{150\text{MHz}} \gtrsim 10$ mJy) are typically active galactic nuclei (Wilman et al. 2008) and are usually visible at 3.4 and $4.6 \mu\text{m}$ unless they lie at high redshift ($z > 1$). There is no IR counterpart to the radio source in any of the WISE bands, further lending weight to the idea that the source is an associated compact remnant.

The data points were estimated by extracting the total integrated flux density within a polygon that tightly enclosed the G23.11+0.18 emission (see Figure 3). A surrounding region, indicated in Figure 4, was used to subtract the flux of the background flux density for each band, while areas containing probable contamination nearby W41 and HII regions were excluded from the calculation. The uncertainties on the flux density measurements are largely driven by the flux calibration accuracy of the data, about 8 % in this region. For more details about this process applied to a large sample of new and known SNRs, see Hurley-Walker (2019b) and Hurley-Walker (2019c).

We obtained a Bonn 11-cm Survey single dish 2.695 GHz image of the region and measured the total flux density of the SNR, integrating over the same area and using the same region as used for background subtraction of the GLEAM data. The signal-to-noise of the SNR is much lower, due to the higher background level from the single dish measurement, and the lower brightness of the SNR at higher frequencies due to its non-thermal spectrum.

As shown in Figure 3, we subtracted the point source from the GLEAM and Effelsberg data, and calculated the 72–2695 MHz radio spectral index⁶ as $\alpha = -0.58 \pm 0.06$, which is within the typical range of SNRs (-0.3 to -0.8 Bozzetto et al. 2017) for a wide range of diameters and ages (5–100 pc and $200\text{--}10^6$ yr, respectively)). Table 1 lists the radio continuum integrated flux densities of G23.11+0.18 and the contaminating point source at each frequency.

⁶ Defined as $S_\nu \propto \nu^\alpha$

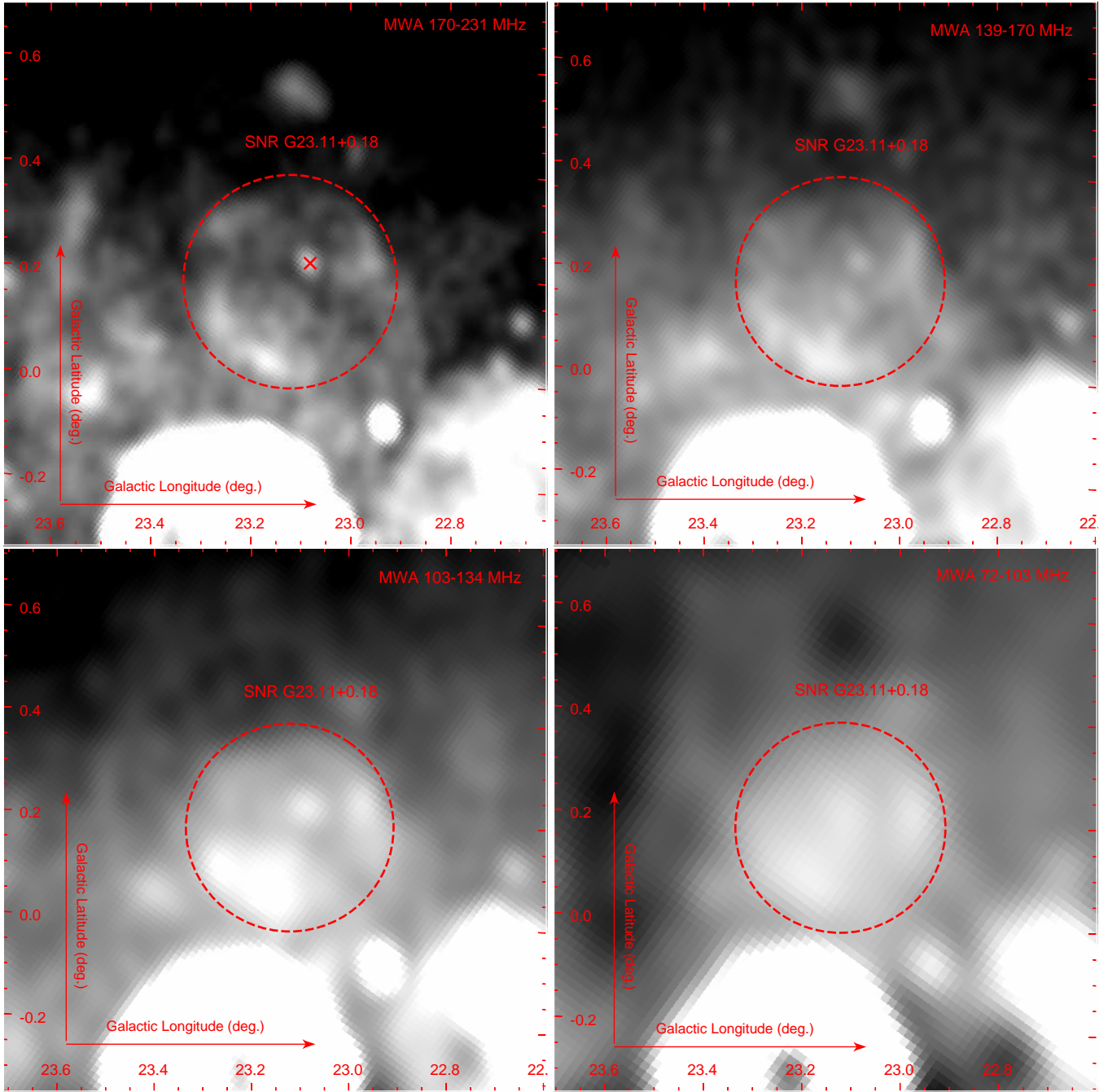


Figure 2. Murchison Widefield Array radio continuum images of the new SNR candidate in 4 wavebands - 170–231, 139–170, 103–134 and 72–103 MHz. A red dashed circle indicates the boundary of SNR candidate 23.1+0.2. In the top left image, the position of the radio continuum point source G23.08+0.22 is indicated by a cross.

3.2. *HESS J1832–085 and a Search for a Gas Association*

Figure 5 shows the HESS Galactic Plane Survey TeV gamma-ray map overlaid on MWA radio continuum data. The unidentified gamma ray source, HESS J1832–085, is coincident with the northern region of the new SNR candidate. As gamma-ray emission associated with SNR shells is not uncommon (e.g. see [H.E.S.S. Collaboration et al. 2018b](#)),

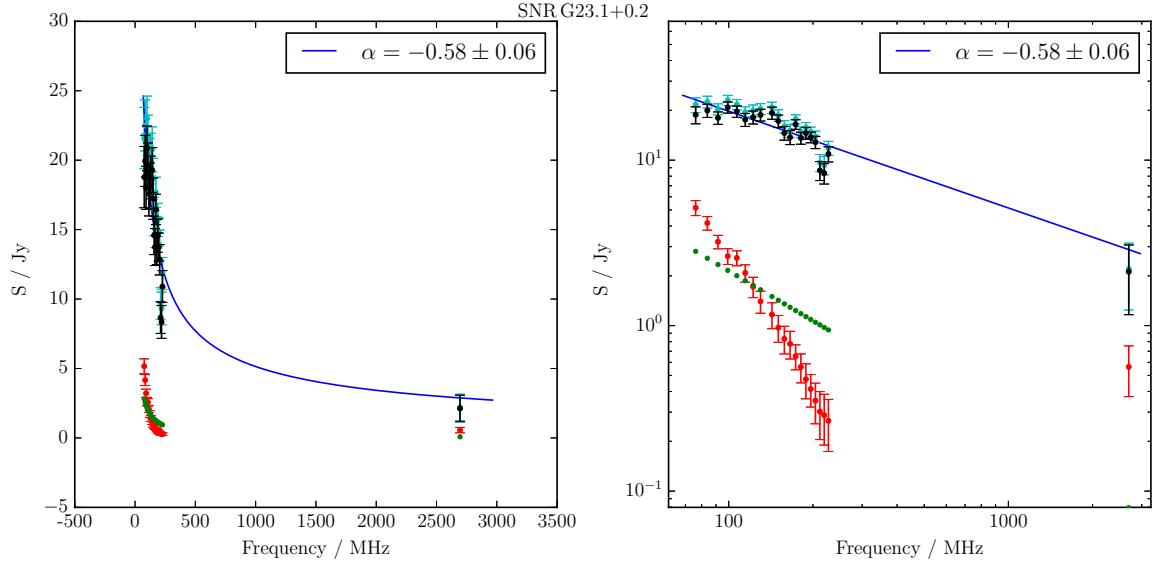


Figure 3. Radio continuum spectra of G23.11+0.18. Linear and log scales are shown on the left and right, respectively. G23.11+0.18 GLEAM and Effelsberg 2.695 GHz flux density measurements are in cyan before the contaminating radio source (green) is subtracted, and black after; the background data points are in red, and the power law trend line fit is in blue.

ν Frequency (MHz)	Total flux density (Jy)	Predicted point source flux density (Jy)	G23.11+0.18 flux density after source-subtraction (Jy)
76	21.6 ± 2.2	2.81 ± 0.14	18.8 ± 2.2
84	22.5 ± 1.8	2.55 ± 0.13	19.9 ± 1.8
92	20.3 ± 1.6	2.34 ± 0.12	18.0 ± 1.6
99	23.0 ± 1.6	2.16 ± 0.11	20.8 ± 1.6
107	21.7 ± 1.6	2.00 ± 0.10	19.7 ± 1.6
115	19.4 ± 1.6	1.87 ± 0.09	17.6 ± 1.6
122	19.9 ± 1.6	1.75 ± 0.09	18.2 ± 1.6
130	20.4 ± 1.5	1.65 ± 0.08	18.8 ± 1.5
143	20.8 ± 1.6	1.50 ± 0.07	19.3 ± 1.6
150	18.7 ± 1.5	1.42 ± 0.07	17.2 ± 1.5
158	15.9 ± 1.4	1.35 ± 0.07	14.6 ± 1.4
166	15.0 ± 1.3	1.29 ± 0.06	13.7 ± 1.3
173	17.7 ± 1.1	1.23 ± 0.06	16.4 ± 1.1
181	14.8 ± 1.1	1.18 ± 0.06	13.6 ± 1.1
189	15.7 ± 1.2	1.13 ± 0.06	14.6 ± 1.2
196	14.8 ± 1.0	1.09 ± 0.05	13.7 ± 1.0
204	13.9 ± 1.1	1.05 ± 0.05	12.8 ± 1.1
212	9.7 ± 1.1	1.01 ± 0.05	8.7 ± 1.1
220	9.3 ± 1.2	0.97 ± 0.05	8.3 ± 1.2
227	11.8 ± 1.1	0.94 ± 0.05	10.9 ± 1.2
2695	2.2 ± 1.0	0.08 ± 0.01	2.1 ± 1.0

Table 1. Radio flux densities derived from MWA data for G23.11+0.18.

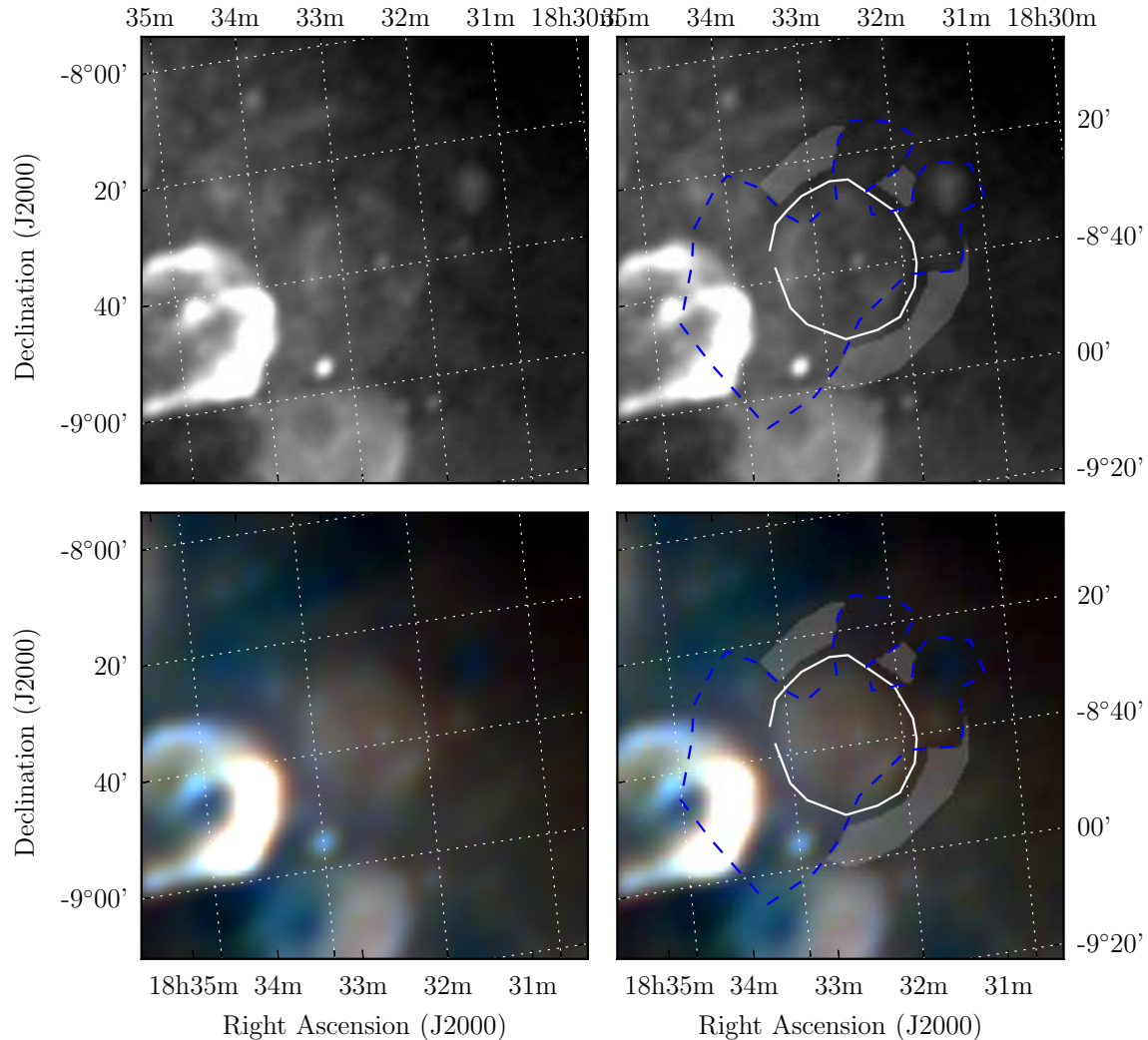


Figure 4. The MWA radio continuum images used for source extraction. The top two images show the 170–231 MHz data while the lower two images show RGB cubes of 72–103 MHz (R), 103–134 MHz (G), and 139–170 MHz (B). The colour scales for the GLEAM RGB cube are 3.5–14.6, 1.5–7.7, and 0.6–4.2 Jy beam⁻¹ for R, G, and B, respectively. In the rightmost images, the white polygon indicates the region used for the G23.11+0.18 flux density estimation, the blue dashed polygon indicates a region excluded from the flux density estimation, and the shaded region indicates the region used to examine the background flux density.

we propose that HESS J1832–085 is likely associated with G23.11+0.18. We further argue that such a coincidence reinforces the candidacy status of G23.11+0.18 as a new Galactic SNR.⁷

A search for molecular gas towards G23.11+0.18 can shed light on SNR nature in three ways. Firstly, among young ($\sim 10^3$ yr) SNRs in the Sedov-Taylor phase, evolution is often seen to be occurring in an inhomogeneous, clumpy medium (e.g. Moriguchi et al. 2005; Zirakashvili & Aharonian 2010; Fukui et al. 2012; Inoue et al. 2012; De Horta et al. 2013; Maxted et al. 2012, 2013a,b; Fukuda et al. 2014; Fukui et al. 2017; Sano et al. 2017; Maxted et al. 2018a,b,c; Sano et al. 2018). It follows that a search for clumps towards the gamma-ray source HESS J1832–085 can provide an insight into its age, environment, and possible relation to G23.11+0.18.

Secondly, gamma-ray emission is observed towards SNRs that are middle-aged ($\sim 10^4$ yr) and in the radiative phase. The gamma-ray emission seems to result from a lingering population of CR protons that diffuse into nearby molecular

⁷ Indeed the independent identification of G23.11+0.18 in two radio continuum data-sets (in this MWA study, and in THOR data, Anderson et al. 2017) is already strong evidence in favour of the shell-like feature.

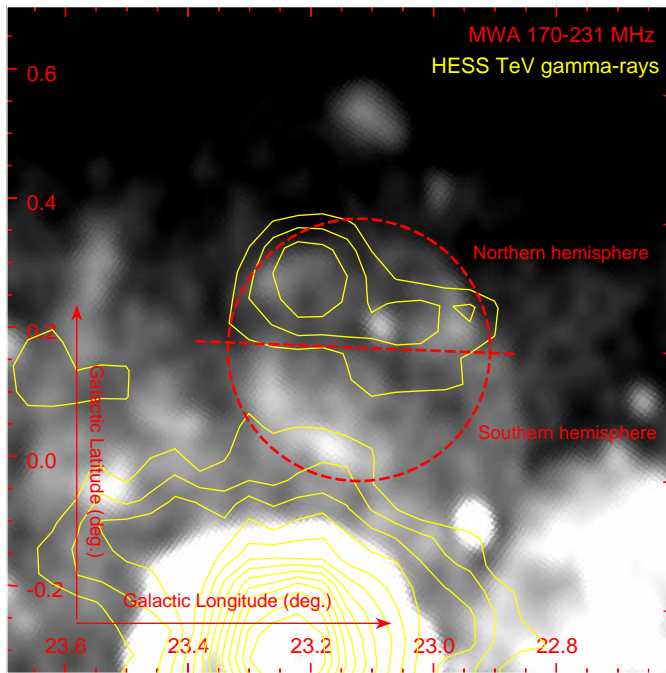


Figure 5. Murchison Widefield Array 170-231 MHz radio continuum image of SNR candidate G23.11+0.18 with HESS TeV Gamma-ray significance contours overlaid (contour increment is 1σ , beginning at 3σ). A red circle indicates the proposed location of G23.11+0.18.

gas (e.g. SNR W28; Arikawa et al. 1999; Aharonian et al. 2008; Gabici et al. 2007, 2008, 2009, 2010; Nicholas et al. 2011, 2012; Maxted et al. 2016, 2017). A search for molecular clouds corresponding to the HESS J1832–085 gamma-ray emission allows us to test if a similar scenario is occurring for G23.11+0.18. In our investigation, this ‘nearby cloud’ scenario might be difficult to distinguish from an ‘embedded clump’ scenario in the case that a nearby inhomogeneous cloud lies adjacent to the SNR in the line of sight.

Finally, the identification of a void or cavity in molecular gas corresponding to similar dimensions to G23.11+0.18 provides a plausible gas association in a progenitor wind-blown bubble scenario.

In the following sections, we examine FUGIN CO, ^{13}CO and $\text{C}^{18}\text{O}(1-0)$ data in a search for both dips in molecular gas corresponding to the new SNR candidate, and gas coincident to the unidentified gamma-ray source HESS J1832–085, which might be candidate embedded clumps or nearby clouds illuminated by CRs. We also perform a search for the SNR candidate in other frequencies.

3.2.1. Galactic Structure towards G23.11+0.18

In Figure 6 we display longitude-velocity plots of the G23.11+0.18 region. The most intense structures in the three CO isotopologue tracers are between 75 and 120 km s^{-1} . These high-velocity components likely correspond to molecular gas near the Norma-arm tangent and the far-side of the Scutum-Crux arm. Three additional line of sight components are indicated: Scutum-Crux-arm (near), Sagittarius arm and local molecular gas. The attribution of names for these structures are extrapolated from Umemoto et al. (2017) and the Milky Way schematic in Figure 6. Although it is possible that components of the far side of the Sagittarius and Perseus arm are present in position-velocity plots, we do not attempt make further inferences about Galactic structure from this data-set, and instead simply focus on associations for G23.11+0.18.

3.2.2. Possible gas signatures of G23.11+0.18

Two void-like structures were identified by eye in velocity-space, and are indicated in Figure 6. Void A is between 80 and 90 km s^{-1} within molecular gas most-likely attributable to the Norma arm. Void B is between 50 and 60 km s^{-1} within molecular gas most-likely attributable to the Scutum arm.

Void A is completely encircled in $^{12}\text{CO}(1-0)$ and $^{13}\text{CO}(1-0)$ emission in velocity-space, while a ~ 0.1 degree gap can be observed in the low-velocity side of C^{18}O emission. Void B is more sparse with ^{12}CO , ^{13}CO and $\text{C}^{18}\text{O}(1-0)$ emission

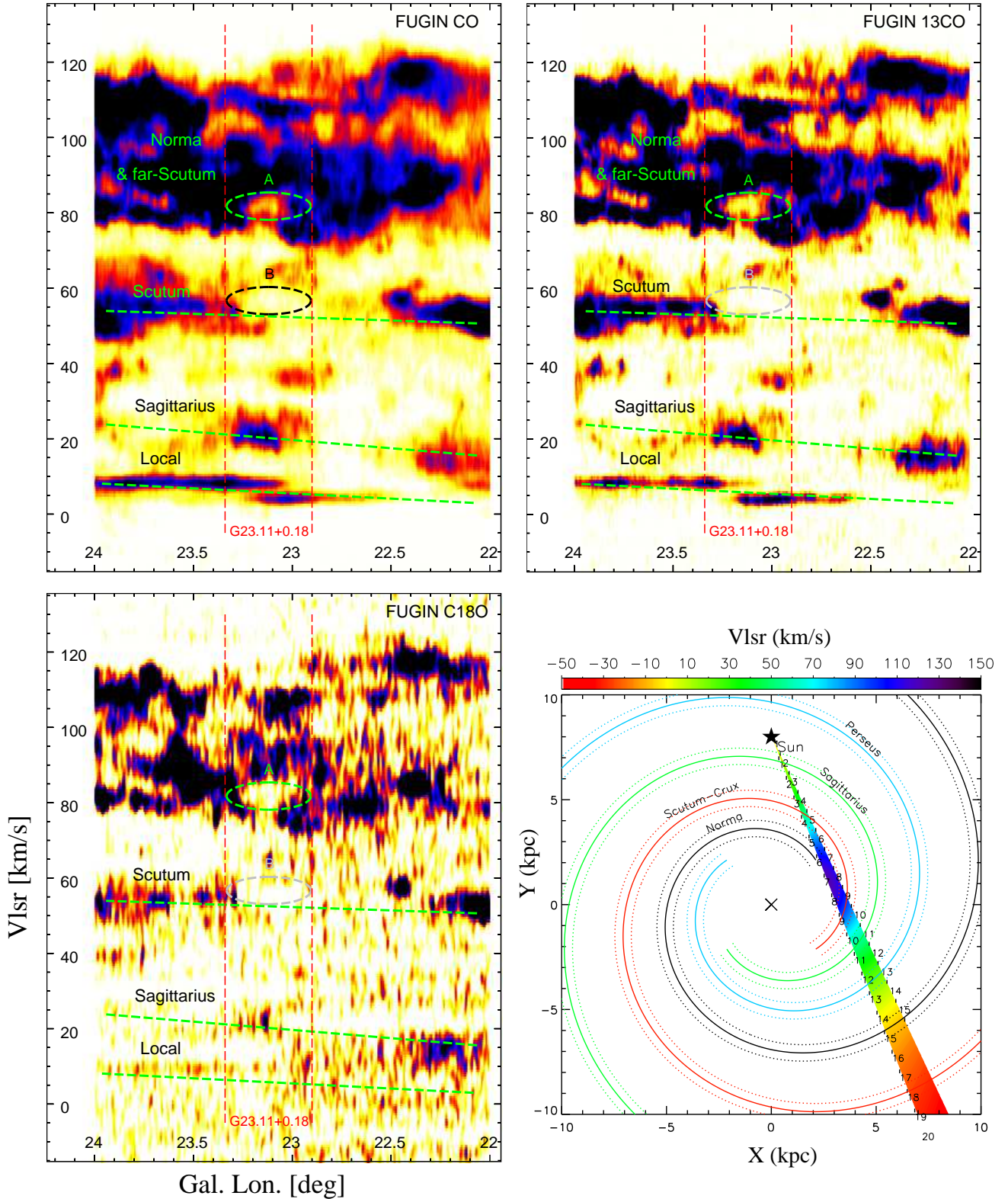


Figure 6. $^{12}\text{CO}(1-0)$, $^{13}\text{CO}(1-0)$ and $\text{C}^{18}\text{O}(1-0)$ emission as a function of Galactic longitude and line of sight velocity (top-left, top-right and bottom-left, respectively). Data have been integrated in the Galactic latitude dimension between 0 and 0.4 degrees, corresponding to the candidate SNR G23.11+0.18. Darkness in colour indicates increasing intensity. Red dashed lines indicate the Longitudinal extent of G23.11+0.18, green dashed lines indicate the approximate locations of Galactic arms, as extrapolated from Figure 8 of Umemoto et al. (2017). Circles indicate two void-candidates, Void A and Void B. On the bottom-right is a schematic of the Galactic arm model in Vallée (2016), where colour is used to indicate kinematic velocity in the direction of this field..

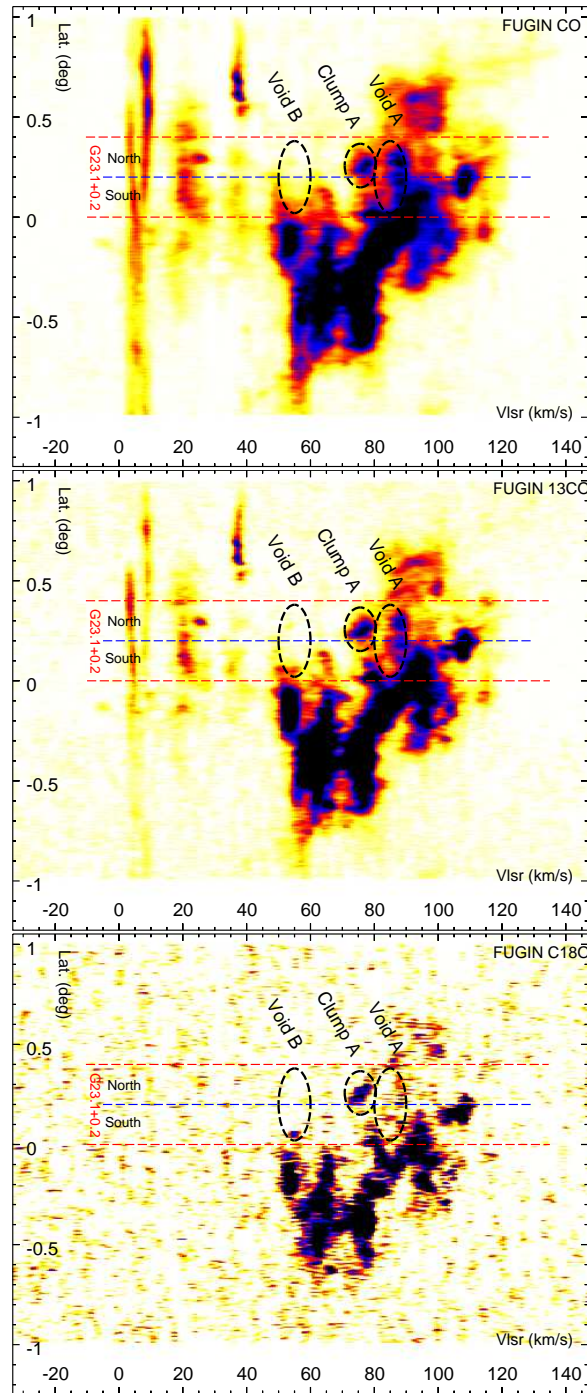


Figure 7. $^{12}\text{CO}(1-0)$, $^{13}\text{CO}(1-0)$ and $\text{C}^{18}\text{O}(1-0)$ emission as a function of Galactic latitude and line of sight velocity. Data have been integrated in the Galactic longitude dimension between 22.9 and 23.34 degrees, corresponding to the candidate SNR G23.11+0.18. Darkness in colour indicates increasing intensity. Red dashed lines indicate the Longitudinal extent of G23.11+0.18, while a blue line indicates the mid-latitude point of the SNR. Two G23.11+0.18 void candidates, Void A and B, and Clump A are indicated with ellipses.

on the higher-longitude side and a central clump on the high velocity side. $^{12}\text{CO}(1-0)$ and $^{13}\text{CO}(1-0)$ emission partially envelopes Void B on both sides in velocity-space. We consider these two void-like structures as possible associations for G23.11+0.18.

In Figure 7 we display latitude-velocity plots of the G23.11+0.18 region. Figure 7 shares some velocity characteristics in common with Figure 6, i.e. structures of Norma, Scutum, Sagittarius and local gas components are likely present.

Imaging the CO data in the latitudinal dimension allows us to investigate correspondence with the unidentified gamma-ray source HESS J1832–085. Since HESS J1832–085 appears in the northern half of G23.11+0.18, we search for velocity ranges that contain significantly more gas in the northern hemisphere of G23.11+0.18 when compared to the southern hemisphere. This analysis carries an assumption that the gamma-ray emission should correlate with gas, as motivated by aforementioned known cases of gas/gamma-ray correlation caused by CRs interacting with molecular clouds (see Section 3.2).

From Figure 7, one velocity range stands out as having significantly more emission in the north relative to the south: 70-80 km s⁻¹. This feature is most prominent in C¹⁸O(1-0) emission, which highlights the most CO(1-0) optically-thick components. We indicate the C¹⁸O(1-0) component as ‘Clump A’ in Figure 7.

From Figure 6 and 7, we have flagged three velocity ranges for us to examine for potential association: two wind-blown void candidates for G23.11+0.18, Void A and B (80-90 km s⁻¹ and 50-60 km s⁻¹, respectively), and one clump association for HESS J1832–085 (Clump A, 70-80 km s⁻¹).

Figure 8, 9 and 10 are 10 km s⁻¹-slices of CO(1-0), ¹³CO(1-0) and C¹⁸O(1-0) emission, respectively. From these figures, the two candidate Void velocity ranges, are morphologically consistent with wind-blown cavity scenarios. The Void A velocity (80-90 km s⁻¹) shows a wall of molecular gas in CO and ¹³CO stretching from the north-east, down to the south-east and around to the south-west to encircle the SNR candidate over ~180°. Within the G23.11+0.18 perimeter, and to the north-west, less intense, and clumpier emission exists. As expected from its relative rarity, C¹⁸O(1-0) is generally less prominent than CO and ¹³CO(1-0) around Void A. There is, however, C¹⁸O(1-0) emission towards the eastern, western and south-western edges of G23.11+0.18, indicating the presence of high CO optical-depth molecular clumps.

The Void B velocity (50-60 km s⁻¹) also exhibits a wall of molecular gas in CO and ¹³CO(1-0). Emission from these two diffuse molecular gas tracers surround the SNR candidates eastern, southern and south-western boundary – approximately 120° of angular correspondence. C¹⁸O(1-0) indicates the presence of optically-thick ¹²CO clumps on the south-eastern and southern G23.11+0.18 boundary.

Clump A (70-80 km s⁻¹) is near the Void A velocity (80-90 km s⁻¹) and may form part of the same arm. The 70-80 km s⁻¹ velocity window in Figure 8 and 9 exhibits CO(1-0) and ¹³CO(1-0) emission overlapping with the north-west and east of G23.11+0.18, while a dip in emission in the south is bordered by emission at the southern edge of G23.11+0.18. C¹⁸O emission is also prominent in the north-west quadrant of G23.11+0.18 and around the south-east and south-west boundaries.

The correspondence of the 70-80 km s⁻¹ CO emission with the HESS J1832–085 gamma-ray emission is incomplete in the north-east of G23.11+0.18, but this significantly improves by including the neighboring Void A velocity of 80-90 km s⁻¹ (see Figure 11). Physically, this can be justified under the assumption that the emission originates from the same arm, with both Void A and Clump A having an association with G23.11+0.18, particularly if local kinematic cloud motions of 5-10 km/s exist. The association is consistent with both a clumpy medium within the G23.11+0.18 shell or gas immediately adjacent to the SNR in the line of sight. In Figure 11, a CO/¹³CO clump is coincident with the TeV gamma-ray peak of HESS J1832–085. From this, we suggest that the initial ‘point-like’ classification of the source is simply reflecting a gamma-ray flux that follows gas distribution inside or near G23.11+0.18.

3.3. Optical and Infrared Searches for G23.11+0.18

We were unable to find morphological signatures of the SNR candidate G23.11+0.18 in H α images taken in 1999 as part of the SuperCOSMOS Sky Survey with the UK-Schmidt telescope (Hambly et al. 2001). Furthermore, we did not find G23.11+0.18 in Midcourse Space Experiment or Spitzer-GLIMPSE infrared data (Price et al. 2001; Churchwell et al. 2009, respectively).

We did, however, find infrared-dark features that match the morphology of molecular gas traced by FUGIN CO. In Figure 11, we display 8 μ m emission with ¹³CO(1-0) emission contours from the 70-90 km s⁻¹ velocity slice overlaid. One ¹³CO clump in the north-west of G23.11+0.18 has a notable corresponding dark-lane association, while several dark lanes lie within ¹³CO-traced gas at the south-eastern boundary. These associations suggest that the gas identified as a potential association for G23.11+0.18 is foreground to a significant number of stars within Galactic plane, hence favouring a near-side solution to the kinematic degeneracy of Galactic rotation in the inner plane. This is an important

FUGIN 12CO(1-0)

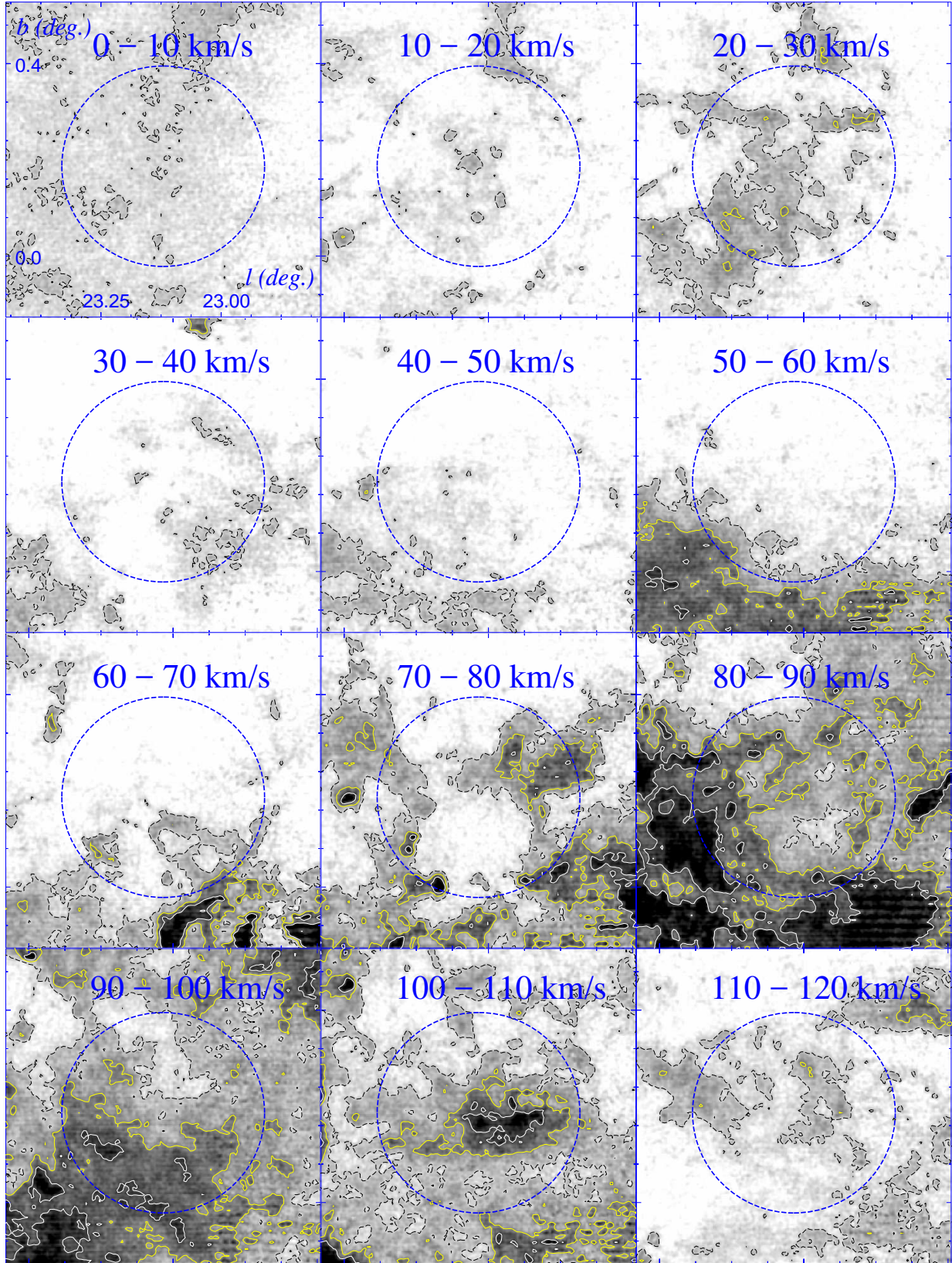


Figure 8. FUGIN $^{12}\text{CO}(1-0)$ integrated intensity images (Umemoto et al. 2017). Darkness in colour indicates increasing intensity. Contour levels showing 20, 40 and 60 K km s^{-1} are overlaid (black-dashed, yellow and white, respectively). Velocity integration ranges are indicated on each image. A circle indicates the approximate location of candidate SNR G23.11+0.18.

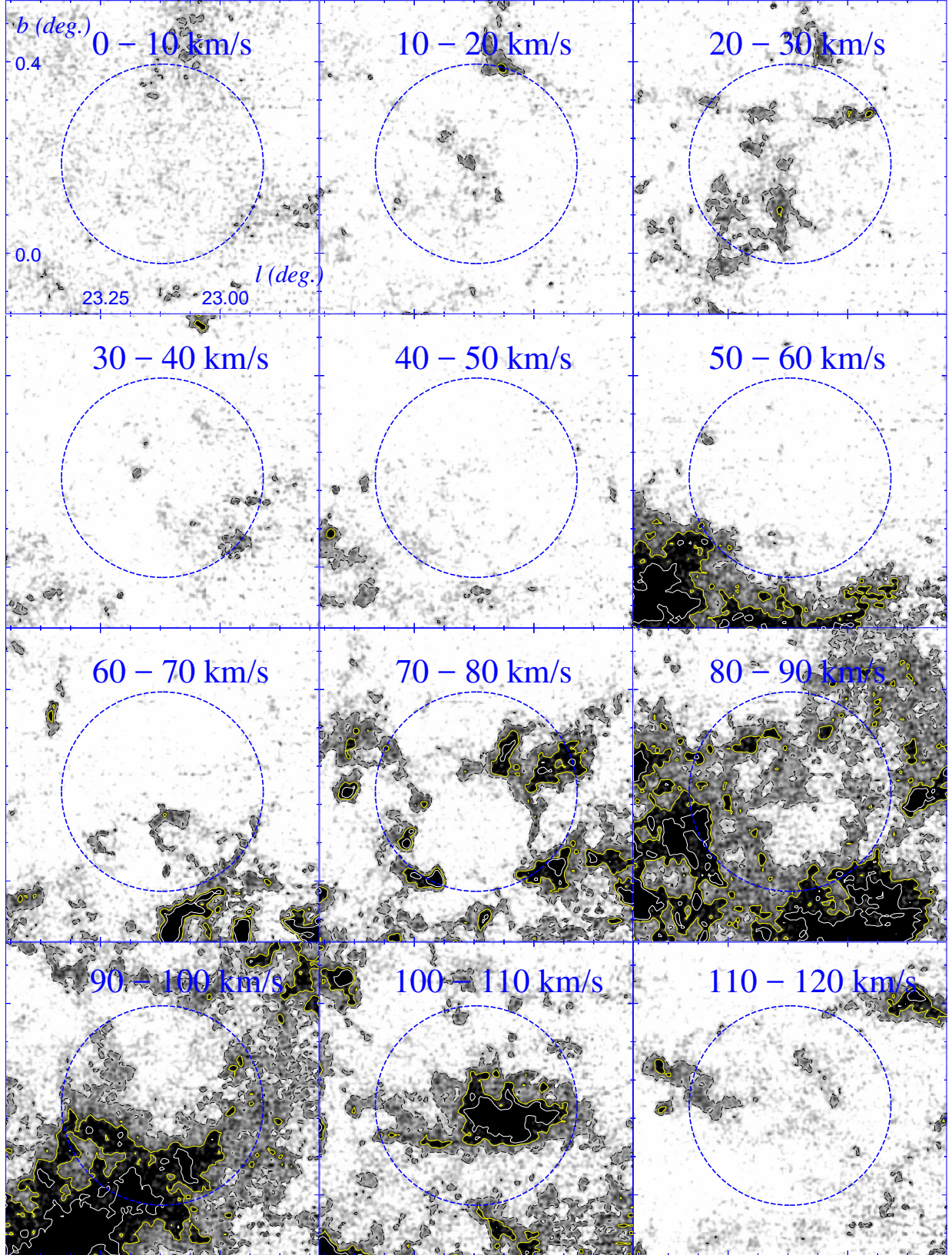
FUGIN $^{13}\text{CO}(1-0)$ 

Figure 9. FUGIN $^{13}\text{CO}(1-0)$ integrated intensity images (Umemoto et al. 2017). Darkness in colour indicates increasing intensity. Contour levels showing 6, 12 and 18 K km s^{-1} are overlaid (black-dashed, yellow and white, respectively). Velocity integration ranges are indicated on each image. A circle indicates the approximate location of candidate SNR G23.11+0.18.

FUGIN C18O(1-0)

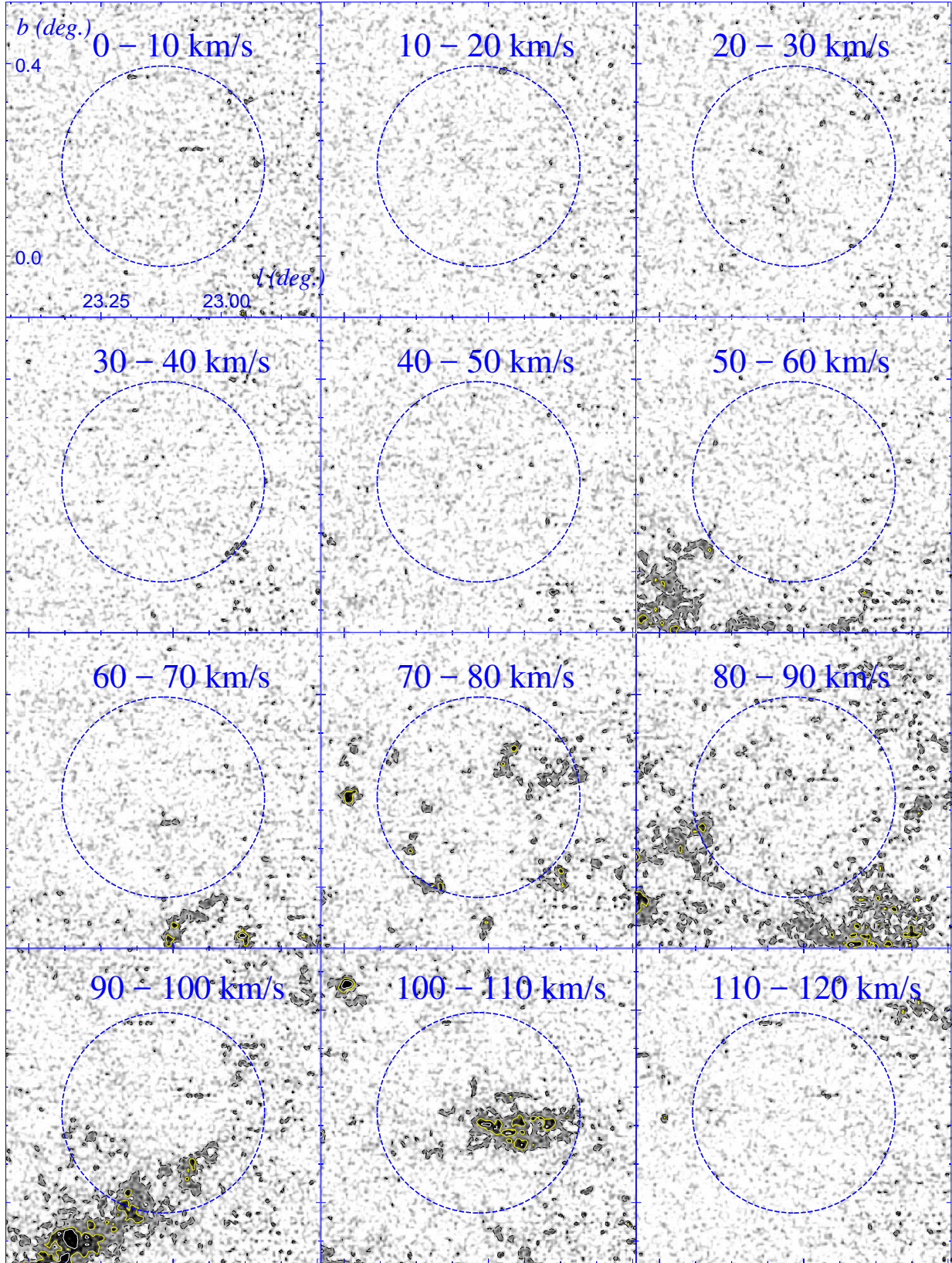


Figure 10. FUGIN C¹⁸O(1-0) integrated intensity images (Umemoto et al. 2017). Darkness in colour indicates increasing intensity. Contour levels showing 3, 6 and 9 K km s⁻¹ are overlaid (black-dashed, yellow and white, respectively). Velocity integration ranges are indicated on each image. A circle indicates the approximate location of candidate SNR G23.11+0.18.

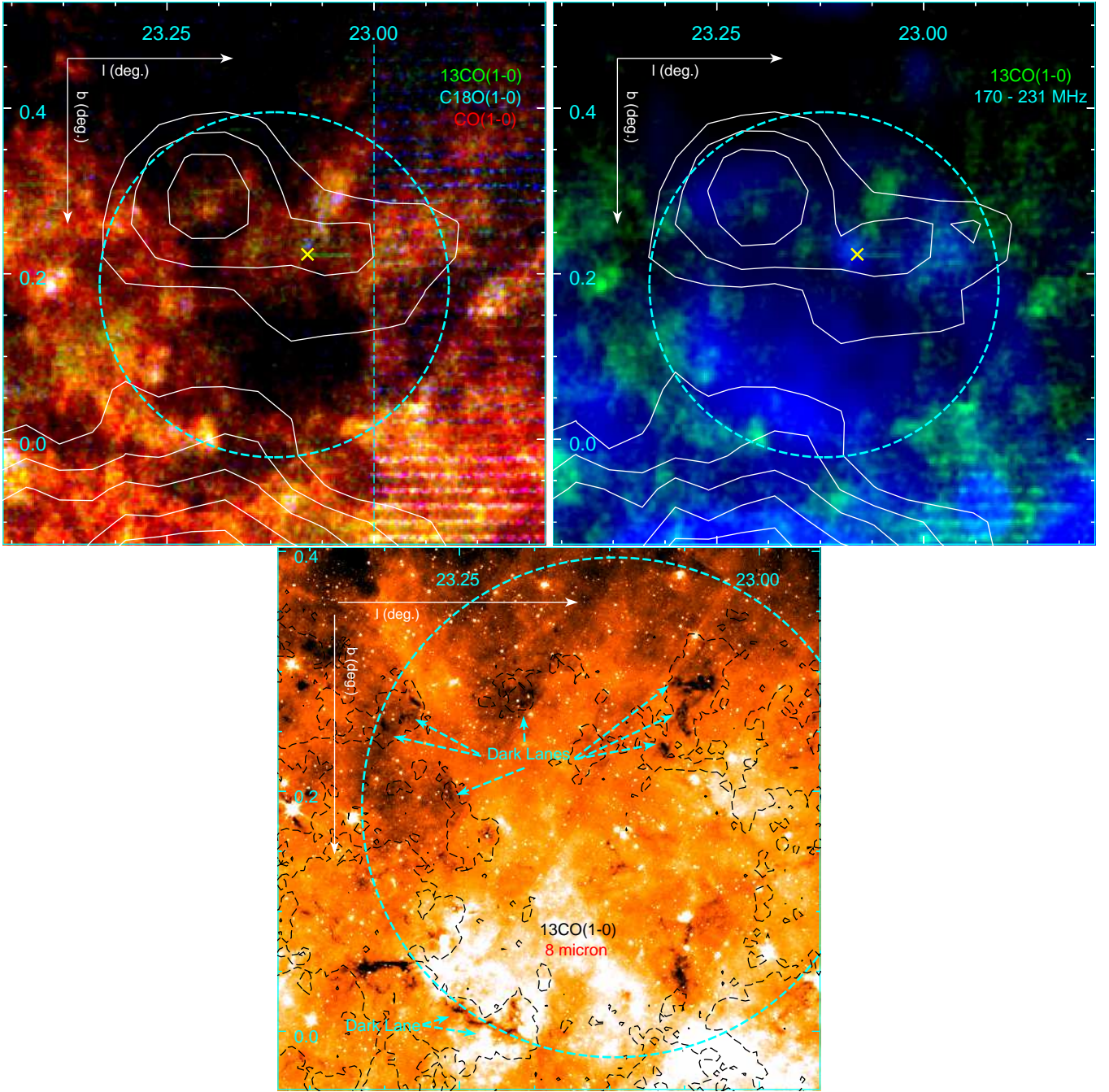


Figure 11. **Top left:** Three-colour image of FUGIN $^{12}\text{CO}(1-0)$ (red), $^{13}\text{CO}(1-0)$ (green), and $\text{C}^{18}\text{O}(1-0)$ (blue) emission, velocity-integrated between 70 and 90 km s^{-1} . HESS 3, 4, 5, 6 and 7σ contours are overlaid. A dashed vertical line indicates the boundary between finalised (left) and preliminary (right) image processing properties. The preliminary data exhibits some striping artefacts. **Top right:** Two-colour image of $^{13}\text{CO}(1-0)$ velocity-integrated between 70 and 90 km s^{-1} (green) and MWA 170-231 MHz radio continuum (blue). HESS 3, 4, 5, 6 and 7σ contours are overlaid. **Bottom** Spitzer $8\mu\text{m}$ infrared emission with overlaid FUGIN $^{13}\text{CO}(1-0)$ 70-90 km s^{-1} emission 15 K km s^{-1} contours. Dark lanes that are morphologically suggestive of association with the $^{13}\text{CO}(1-0)$ emission is indicated.

clue for determining the SNR distance, because we expect components of the near and far Norma-arms to be confused with the far-Scutum-Crux arm for velocities above $\sim 75 \text{ km/s}$ (e.g. see Figure 6).

3.4. A Search for G23.11+0.18 in X-rays

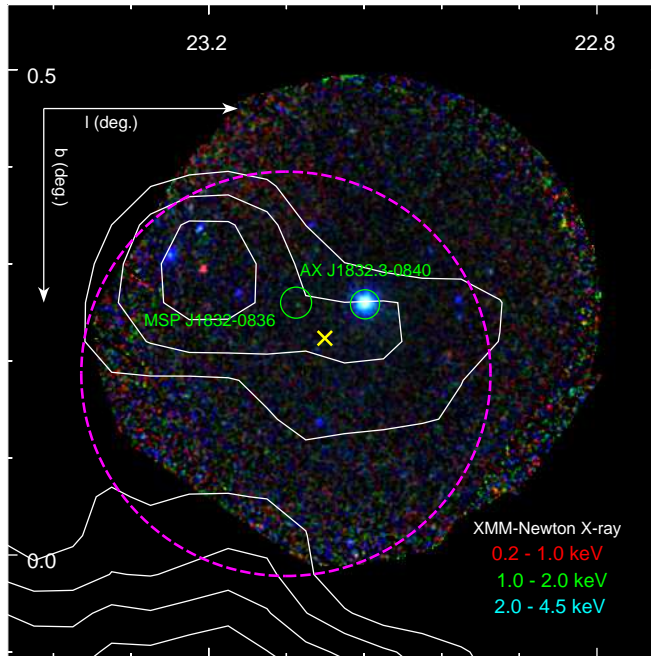


Figure 12. The *XMM-Newton* three-colour image showing 0.2-1, 1.0-2.0 and 2.0-4.5 keV bands in red, green and blue, respectively. HESS 3, 4 and 5σ >1 TeV gamma-ray emission contours are overlaid (Abdalla et al. 2018). The position of G23.11+0.18 is indicated by a broken magenta circle. The positions of the cataclysmic variable star AX J1832.3-0840 and millisecond pulsar MSP J1832–0.836 (Lee et al. 2018) are indicated by green circles. A yellow cross marks the radio continuum source possibly associated with G023.090+0.220

In an attempt to establish the G23.11+0.18 candidacy as an SNR, we examined *XMM-Newton* X-ray data. In Figure 12, we present X-ray images of the 0.2-1 keV, 1.0-2.0 keV and 2.0-4.5 keV bands, which represent ‘soft’, ‘medium’ and ‘hard’ X-ray emission, respectively. No significant diffuse X-ray emission is seen in the images, or in higher energy bands of ~ 4.5 -10 keV, and we are unable to reinforce the evidence in favour of the SNR candidate G23.11+0.18 using this X-ray data-set. We attribute this to a likely high level of foreground absorption (see Section 3.4).⁸

3.5. The Nature and Distance of G23.11+0.18

In Section 3.2, we examined position-velocity plots to identify two voids in molecular gas, Void A in the Norma arm and Void B in the Scutum-Crux arm. We suggested these to be associations for SNR candidate G23.11+0.18. Then, under the assumption that the gamma-ray source HESS J1832–085 is associated with the SNR, we suggested that gas in the velocity range neighboring Void A is also associated with G23.11+0.18, which would favour the Void A association interpretation for G23.11+0.18 over Void B. Furthermore, the Void B interpretation is disfavoured by the possibility that one side of this structure may in fact be part of a confused far-side Galactic arm - the far-Sagittarius arm, perhaps tentatively observed in Figure 6 at ~ 65 km s^{-1} . With this, and the lack of gamma-ray/gas correspondence in the Scutum-Crux arm in mind, we move forward with a Clump A-Void A G23.11+0.18 association hypothesis.

The proposed scenario presents a consistent picture that unifies the radio continuum remnant, the gamma-ray source and the ISM. In this interpretation, the wind of the G23.11+0.18 progenitor star blows-out a cavity in nascent Norma-arm molecular gas before exploding within the region evacuated of diffuse gas. The supernova remnant shell, seen in radio continuum, expands to interact with clumps remaining within the cavity and eventually the cavity wall. Particle acceleration occurs and initiates gamma-ray emission, which may either correspond to escaping CR hadrons interacting with northern clouds (e.g. Aharonian et al. 2008) adjacent in the line of sight, or CR hadrons interacting with clumps within the SNR shell (e.g. Fukui et al. 2012). Both of these scenarios are consistent with a hadronic gamma-ray emission mechanism for G23.11+0.18. A leptonic scenario may also be consistent with the proposed ISM association if the population of high energy electrons is boosted in regions where the SNR shock meets northern gas, as briefly

⁸ We note that a large number of prominent radio SNRs are not readily detected in X-ray images (e.g. Crawford et al. 2010).

suggested by [Susch et al. \(2018\)](#) for the young SNR Vela Jr. In the Vela Jr case, however, TeV gamma-ray emission was accompanied by strong non-thermal X-ray emission from the same population of $>$ TeV electrons - something not seen in G23.11+0.18, which may have a less-energetic population of electrons due to a larger age, as modelled below. In either case (leptonic or hadronic), the Clump A-Void A G23.11+0.18 association hypothesis is consistent irrespective of the gamma-ray emission mechanism.

Assuming a Milky Way Galactic centre distance and Galactic rotation Velocity of 8 kpc and 230 km s^{-1} , respectively (see [Vallée 2017](#)), we estimate the kinematic distance of the Void A+Clump A gas ($70\text{-}90 \text{ km s}^{-1}$) to be $4.6\pm 0.8 \text{ kpc}$ ([Brand & Blitz 1993](#)), where the distance range corresponds to the velocity ranges of the features in question, while the statistical error of 0.4 kpc corresponds to 10 km s^{-1} (conservatively estimated as the expectation for local gas motions). Here, we are assuming the near-side solution, due to the presence of dark lanes morphologically matching the $70\text{-}90 \text{ km s}^{-1}$ gas (see Section 3.3). There is some inconsistency between the calculated kinematic distance of $4.6\pm 0.8 \text{ kpc}$, and the schematic in Figure 6, which would place gas at this distance between Galactic arms. In contrast, we consider the ordering and velocity of clear, significant Galactic arms in the position-velocity plots to be a more reliable tool for assigning a Galactic arm to the $70\text{-}90 \text{ km s}^{-1}$ gas, in this case the Norma arm.

Under the assumption of an association between the SNR candidate G23.11+0.18 and the CO-traced molecular gas of the Norma-arm, the $4.6\pm 0.8 \text{ kpc}$ distance can also be applied to G23.11+0.18, to derive a SNR diameter of $31.5\pm 7.9 \text{ pc}$ (for a SNR angular diameter of $21.7\text{-}25.0'$, and including the kinematic distance uncertainty). Furthermore, the wind-blown bubble nature implied by such an association would mean that the SNR originates from a core-collapse progenitor event.

We model the feasibility of this scenario using SNR evolution modeling software by [Leahy & Williams \(2017\)](#), which primarily utilises the approach outlined in [Truelove & McKee \(1999\)](#). We assume a low explosion energy of $0.5\times 10^{51} \text{ erg}$, consistent with a core-collapse event.⁹

With the assumed diameter of $31.5\pm 7.9 \text{ pc}$, the SNR age could range from 2.1-5.2 kyr if the evolution takes place in an evacuated medium of homogeneous density 0.01 cm^{-3} , to an age of 8.6-54 kyr if inside a dense 1.0 cm^{-3} medium. In the former case, strong non-thermal X-ray emission would be produced from a population of 1-10 keV electrons within the fast $>1000 \text{ km s}^{-1}$ Sedov-Taylor-phase shocks of G23.11+0.18, while the latter case would result in a significant 10-100 eV thermal X-ray component as radiative-phase shocks slow to velocities of $100\text{-}300 \text{ km s}^{-1}$ range. Such soft X-ray emission, however, might be difficult to detect due to high foreground photoelectric absorption (see Section 2.4). The non-detection of strong non-thermal emission in *XMM-Newton* data, including above $\sim 5 \text{ keV}$ where photoelectric absorption is negligible, favours a middle age ($\sim 10^4 \text{ yr}$) for G23.11+0.18. G23.11+0.18 is thus probably not similar to the young, $\sim 10^3 \text{ yr}$ -age, radio-dim, gamma-ray-bright shell-type SNRs such as RX J1713.7-3946 or Vela Jr¹⁰. If G23.11+0.18 originated from a similar type of core-collapse explosion into an evacuated cavity, the SNR is likely now at a more-advanced stage of evolution, consistent with the larger diameter ($\sim 32 \text{ pc}$) at the proposed distance of the CO(1-0) void ($\sim 4.6 \text{ kpc}$). Furthermore, the lack of non-thermal keV emission towards G23.11+0.18 indicates that a substantial population of $>1 \text{ TeV}$ electrons is not present in the region, thus disfavouring a leptonic scenario for gamma-ray emission, adding weight to the proposed existence of a residual population of $>$ TeV CR protons.

No GeV gamma-ray detection is recorded towards G23.11+0.18 in the most recent Fermi-LAT catalogue ([Acero et al. 2015b](#)). The HESS J1832-085 $>1 \text{ TeV}$ spectral index is 2.38 ± 0.14 , consistent with HESS TeV gamma-ray shells such as Vela Jr, RX J1713.7-3946, HESS J1731-347, RCW 86, SN 1006 and HESS J1534-571 which have TeV spectral indices of 2.3-2.5 (e.g. see Tables 4 and 6 of [H.E.S.S. Collaboration et al. 2018a](#)). The flux of HESS J1832-085, however, is $0.9\pm 0.2\% \text{ Crab}^{11}$ - smaller than these HESS TeV shells. For comparison, if HESS J1832-085 is indeed at the distance of $4.6\pm 0.8 \text{ kpc}$, its $>1 \text{ TeV}$ luminosity is $\sim 20\text{-}35\%$ that of RX J1713.7-3946.

We caution the reader that the proposed association between the SNR candidate, gamma-ray source and ISM might simply be a line-of-sight effect in a scenario where the HESS J1832-085 gamma-ray emission originates from runaway CRs produced by SNR W41 rather than SNR candidate G23.11+0.18 (see Section 1.1). This scenario is not favoured by the CO distribution at any line-of-sight velocity in an isotropic CR diffusion scenario, but might still be feasible if anisotropic diffusion effects disproportionately increase the CR density directly north of W41, possibly due to an ordered magnetic-field structure (e.g. [Nava & Gabici 2013](#); [Lau et al. 2017](#)).

⁹ We also assume an ejecta mass of $2 M_{\odot}$ - a parameter that subsequent results are much less sensitive to than explosion energy and ISM density.

¹⁰ We further note that the group of TeV SNR shells ([H.E.S.S. Collaboration et al. 2018a](#)), which G23.11+0.18 may be a part of, are prominent examples where SNR evolution is not fully understood.

¹¹ $>1 \text{ TeV}$ gamma-ray fluxes are often expressed as a fraction of the TeV-bright Crab SNR, e.g. see [Aharonian et al. \(2006\)](#).

Finally, we note that the pulsar PSR J1832–0827 (HESS Collaboration et al. 2015), is at a distance of ~ 4.9 kpc (Cordes & Lazio 2002, also see Clifton & Lyne 1986; Frail et al. 1991) - compatible with the ISM association suggested by our study. The characteristic age of ~ 200 kyr (as estimated from the spin-down luminosity and braking index, Hobbs et al. 2004; Johnston & Galloway 1999), however, is not consistent with a G23.11+0.18 association. At such an age the SNR would likely be beyond the radiative phase and merged with the ISM,¹² hence not detectable. The pulsar ages calculated from spin-down luminosity, however, are generally not reliable measures of real age, because energy loss-rates are not expected to be constant due to likely variations in magnetic field strength (e.g. see Chanmugam et al. 1995) and cases of inconsistency between SNR age and pulsar spin-down age are well-known (e.g. Gotthelf & Halpern 2009). Furthermore, the prospect of the pulsar being ‘spun-up’ complicates the age estimate further. For these reasons, we do not rule-out an association between G23.11+0.18 and PSR J1832–0827.

4. CONCLUSION

We present an examination of the new Galactic SNR candidate G23.11+0.18. MWA radio continuum data indicate a shell-like morphology and a spectral index of $\alpha = -0.63 \pm 0.05$, while the coincident TeV gamma-ray source HESS J1832–085 towards the northern hemisphere of G23.11+0.18 confirms that the object is a likely SNR and viably accelerating particles to super-TeV energies. We conduct an investigation into the nature of the source using archival data. Although we find no corresponding X-ray, infrared or optical emission, based on morphological considerations we propose an association with molecular gas at a kinematic distance of 4.6 ± 0.8 kpc. We propose that a dip in CO-traced molecular gas at a line-of-sight velocity of ~ 85 km s⁻¹ is the G23.11+0.18 progenitor wind-blown bubble, while good correspondence between HESS J1832–085 and gas at a neighbouring velocity is consistent with a gamma-ray production mechanism that involves gas, perhaps p-p interactions by cosmic rays, towards the north of the remnant.

5. ACKNOWLEDGEMENTS

This work is supported by the Australian Research Council grants FT170100243 and FT160100028 and makes use of the Murchison Radio-astronomy Observatory, operated by CSIRO. We acknowledge the Wajarri Yamatji people as the traditional owners of the Observatory site. Support for the operation of the MWA is provided by the Australian Government (NCRIS), under a contract to Curtin University administered by Astronomy Australia Limited. We acknowledge the Pawsey Supercomputing Centre which is supported by the Western Australian and Australian Governments. This work was compiled in the very useful free online LaTeX editor Overleaf. Finally, we thank the anonymous referee, who provided very constructive and helpful comments that improved the quality of our manuscript.

Software: *Miriad* (Sault et al. 1995), *ds9* visualization application (Joye & Mandel 2003), The *Karma* package (Gooch 1995, 1996).

¹² As can be observed by exploring both reasonable and unreasonable parameter spaces using the Leahy & Williams (2017) SNR evolution modelling software.

REFERENCES

- Abdalla, H., Abramowski, A., Aharonian, F., et al. 2018, *A&A*, 612, A1
- Abramowski, A., Aharonian, F., Benkhali, F. A., et al. 2016, *Nature*, 531, 476
- Acero, F., Lemoine-Goumard, M., Renaud, M., et al. 2015a, *A&A*, 580, A74
- Acero, F., Ackermann, M., Ajello, M., et al. 2015b, *ApJS*, 218, 23
- Ackermann, M., Ajello, M., Allafort, A., et al. 2013, *Science*, 339, 807
- Aharonian, F., Akhperjanian, A. G., Bazer-Bachi, A. R., et al. 2006, *A&A*, 457, 899
- Aharonian, F., et al. 2008, *A&A*, 481, 401
- Albert, J., Aliu, E., Anderhub, H., et al. 2007, *The Astrophysical Journal Letters*, 664, L87
- Anderson, L. D., Wang, Y., Bihl, S., et al. 2017, *A&A*, 605, A58
- Arikawa, Y., Tatematsu, K., Sekimoto, Y., & Takahashi, T. 1999, *PASJ*, 51, L7
- Bozzetto, L. M., Filipović, M. D., Vukotić, B., et al. 2017, *ApJS*, 230, 2
- Braiding, C., Wong, G. F., Maxted, N., Burton, M. G., & Blackwell, R. 2018, *PASA*
- Braiding, C., Burton, M. G., Blackwell, R., et al. 2015, *PASA*, 32, e020
- Brand, J., & Blitz, L. 1993, *A&A*, 275, 67
- Brogan, C. L., Gelfand, J. D., Gaensler, B. M., Kassim, N. E., & Lazio, T. J. W. 2006, *ApJL*, 639, L25
- Burton, M. G., Braiding, C., Glueck, C., et al. 2013, *PASA*, 30, e044
- Celli, S., Morlino, G., Gabici, S., & Aharonian, F. 2018, *arXiv e-prints*, arXiv:1804.10579
- Chanmugam, G., Rajasekhar, A., & Young, E. J. 1995, *MNRAS*, 276, L21
- Churchwell, E., Babler, B. L., Meade, M. R., et al. 2009, *PASP*, 121, 213
- Clifton, T. R., & Lyne, A. G. 1986, *Nature*, 320, 43
- Condon, J. J., Cotton, W. D., Greisen, E. W., et al. 1998, *AJ*, 115, 1693
- Cordes, J. M., & Lazio, T. J. W. 2002, *ArXiv Astrophysics e-prints*, astro-ph/0207156
- Crawford, E. J., Filipović, M. D., Haberl, F., et al. 2010, *A&A*, 518, A35
- Cui, Y., Pühlhofer, G., & Santangelo, A. 2016, *A&A*, 591, A68
- De Horta, A. Y., Collier, J. D., Filipović, M. D., et al. 2013, *MNRAS*, 428, 1980
- Eger, P., Laffon, H., Bordas, P., et al. 2016, *MNRAS*, 457, 1753
- Ergin, T., Katsuda, S., Sezer, A., et al. 2017, in *Proceedings of the 7th International Fermi Symposium*, held 15-20 October 2017, in Garmisch-Partenkirchen, Germany (IFS2017), 101
- Frail, D. A., Cordes, J. M., Hankins, T. H., & Weisberg, J. M. 1991, *ApJ*, 382, 168
- Fukuda, T., Yoshiike, S., Sano, H., et al. 2014, *ApJ*, 788, 94
- Fukui, Y., Sano, H., Sato, J., et al. 2012, *ApJ*, 746, 82
- . 2017, *ApJ*, 850, 71
- Gabici, S., Aharonian, F., & Blasi, P. 2007, *Ap&SS*, 309, 365
- Gabici, S., Aharonian, F. A., & Casanova, S. 2009, *MNRAS*, 396, 1629
- Gabici, S., Casanova, S., & Aharonian, F. 2008, in *American Institute of Physics Conference Series*, Vol. 1085, American Institute of Physics Conference Series, ed. F. Aharonian, W. Hofmann, & F. Rieger, 265–268
- Gabici, S., Casanova, S., Aharonian, F., & Rowell, G. 2010, in *SF2A-2010: Proceedings of the Annual meeting of the French Society of Astronomy and Astrophysics*, ed. S. Boissier, M. Heydari-Malayeri, R. Samadi, & D. Valls-Gabaud, 313
- Gaia Collaboration, Brown, A. G. A., Vallenari, A., et al. 2018, *A&A*, 616, A1
- Gooch, R. 1995, in *Astronomical Society of the Pacific Conference Series*, Vol. 77, *Astronomical Data Analysis Software and Systems IV*, ed. R. A. Shaw, H. E. Payne, & J. J. E. Hayes, 144
- Gooch, R. 1996, in *Astronomical Society of the Pacific Conference Series*, Vol. 101, *Astronomical Data Analysis Software and Systems V*, ed. G. H. Jacoby & J. Barnes, 80
- Gotthelf, E. V., & Halpern, J. P. 2009, *ApJL*, 695, L35
- Güver, T., & Özel, F. 2009, *MNRAS*, 400, 2050
- Hambly, N. C., MacGillivray, H. T., Read, M. A., et al. 2001, *MNRAS*, 326, 1279
- HESS Collaboration, Abramowski, A., Acero, F., et al. 2015, *MNRAS*, 446, 1163
- H.E.S.S. Collaboration, Abdalla, H., Abramowski, A., et al. 2018a, *A&A*, 612, A8
- . 2018b, *A&A*, 612, A3
- Hobbs, G., Lyne, A. G., Kramer, M., Martin, C. E., & Jordan, C. 2004, *MNRAS*, 353, 1311
- Hurley-Walker, N. 2019a, *PASA*(submitted), 001, 0001
- . 2019b, *PASA*(submitted), 001, 0001
- . 2019c, *PASA*(submitted), 001, 0001
- Hurley-Walker, N., Callingham, J. R., Hancock, P. J., et al. 2017, *MNRAS*, 464, 1146
- Inoue, T. 2019, *ApJ*, 872, 46

- Inoue, T., Yamazaki, R., Inutsuka, S.-i., & Fukui, Y. 2012, *ApJ*, 744, 71
- Intema, H. T., Jagannathan, P., Mooley, K. P., & Frail, D. A. 2017, *A&A*, 598, A78
- Johnston, S., & Galloway, D. 1999, *MNRAS*, 306, L50
- Joye, W. A., & Mandel, E. 2003, in *Astronomical Society of the Pacific Conference Series*, Vol. 295, *Astronomical Data Analysis Software and Systems XII*, ed. H. E. Payne, R. I. Jedrzejewski, & R. N. Hook, 489
- Kaur, R., Wijnands, R., Paul, B., Patruno, A., & Degenaar, N. 2010, *MNRAS*, 402, 2388
- Lau, J. C., Rowell, G., Burton, M. G., et al. 2017, *MNRAS*, 464, 3757
- Leahy, D. A., & Williams, J. E. 2017, *AJ*, 153, 239
- Lee, J., Hui, C. Y., Takata, J., et al. 2018, *The Astrophysical Journal*, 864, 23.
<http://stacks.iop.org/0004-637X/864/i=1/a=23>
- Maxted, N., de Wilt, P., Rowell, G., et al. 2016, *MNRAS*, 462, 532
- Maxted, N., Rowell, G., de Wilt, P., et al. 2017, *AIP Conference Proceedings*, 1792, 040034.
<http://aip.scitation.org/doi/abs/10.1063/1.4968938>
- Maxted, N., Rowell, G., Dawson, B., et al. 2012, *MNRAS*, 422, 2230
- . 2013a, *PASA*, 30, e055
- . 2013b, *MNRAS*, 434, 2188
- Maxted, N., Burton, M., Braiding, C., et al. 2018a, *MNRAS*, 474, 662
- Maxted, N. I., Braiding, C., Wong, G. F., et al. 2018b, *MNRAS*, 480, 134
- Maxted, N. I., Filipović, M. D., Sano, H., et al. 2018c, *ApJ*, 866, 76
- Minamidani, T., Nishimura, A., Miyamoto, Y., et al. 2016, in *Proc. SPIE*, Vol. 9914, *Millimeter, Submillimeter, and Far-Infrared Detectors and Instrumentation for Astronomy VIII*, 99141Z
- Mori, K., Gotthelf, E. V., Hailey, C. J., et al. 2017, *ApJ*, 848, 80
- Moriguchi, Y., Tamura, K., Tawara, Y., et al. 2005, *ApJ*, 631, 947
- Nava, L., & Gabici, S. 2013, *MNRAS*, 429, 1643
- Nicholas, B., Rowell, G., Burton, M. G., et al. 2011, *MNRAS*, 411, 1367
- Nicholas, B. P., Rowell, G., Burton, M. G., et al. 2012, *MNRAS*, 419, 251
- Price, S. D., Egan, M. P., Carey, S. J., Mizuno, D. R., & Kuchar, T. A. 2001, *AJ*, 121, 2819
- Reich, W., Fuerst, E., Haslam, C. G. T., Steffen, P., & Reif, K. 1984, *A&AS*, 58, 197
- Sano, H., Reynoso, E. M., Mitsuishi, I., et al. 2017, *Journal of High Energy Astrophysics*, 15, 1
- Sano, H., Rowell, G., Reynoso, E. M., et al. 2018, arXiv e-prints, arXiv:1805.10647
- Sault, R. J., Teuben, P. J., & Wright, M. C. H. 1995, in *Astronomical Society of the Pacific Conference Series*, Vol. 77, *Astronomical Data Analysis Software and Systems IV*, ed. R. A. Shaw, H. E. Payne, & J. J. E. Hayes, 433
- Schlafly, E. F., & Finkbeiner, D. P. 2011, *ApJ*, 737, 103
- Strüder, L., Briel, U., Dennerl, K., et al. 2001, *A&A*, 365, L18. http://cdsads.u-strasbg.fr/cgi-bin/nph-bib_query?bibcode=2001A%26A...365L..18S&db_key=AST
- Stupar, M., Parker, Q. A., & Filipović, M. D. 2007a, *MNRAS*, 374, 1441
- Stupar, M., Parker, Q. A., Filipović, M. D., et al. 2007b, *MNRAS*, 381, 377
- Sturm, R., Haberl, F., Pietsch, W., et al. 2013, *A&A*, 558, A3
- Su, Y., Yang, J., Zhou, X., Zhou, P., & Chen, Y. 2014, *ApJ*, 796, 122
- Susch, I., et al. 2018, *ApJ*, 000, 000
- Tingay, S. J., Goeke, R., Bowman, J. D., et al. 2013, *PASA*, 30, e007
- Truelove, J. K., & McKee, C. F. 1999, *ApJS*, 120, 299
- Turner, M. J. L., Abbey, A., Arnaud, M., et al. 2001, *A&A*, 365, L27.
http://cdsads.u-strasbg.fr/cgi-bin/nph-bib_query?bibcode=2001A%26A...365L..27T&db_key=AST
- Umamoto, T., Minamidani, T., Kuno, N., et al. 2017, *PASJ*, 69, 78
- Vallée, J. P. 2016, *AJ*, 151, 55
- . 2017, *Ap&SS*, 362, 79
- Wayth, R. B., Lenc, E., Bell, M. E., et al. 2015, *PASA*, 32, e025
- Wilman, R. J., Miller, L., Jarvis, M. J., et al. 2008, *MNRAS*, 388, 1335
- Wright, E. L., Eisenhardt, P. R. M., Mainzer, A. K., et al. 2010, *AJ*, 140, 1868
- Zhu, H., Tian, W., Li, A., & Zhang, M. 2017, *MNRAS*, 471, 3494
- Zirakashvili, V. N., & Aharonian, F. A. 2010, *ApJ*, 708, 965